

Crystal host engineering for transition metal lasers

Jonathan W. Evans[Ⓞ],^{a,*} Sean A. McDaniel,^b Ronald W. Stites,^b
Patrick A. Berry,^b Gary Cook,^b Thomas R. Harris,^c
and Kenneth L. Schepler[Ⓞ]^d

^aAir Force Institute of Technology, Engineering Physics Department,
Wright-Patterson Air Force Base, Ohio, United States

^bAir Force Research Laboratory, Sensors Directorate,
Wright-Patterson Air Force Base, Ohio, United States

^cAzimuth Corporation, Beavercreek, Ohio, United States

^dUniversity of Central Florida, CREOL, Orlando, Florida, United States

Abstract. Much progress has been made in the power and energy scaling of mid-infrared lasers based on transition metal ions, such as Cr^{2+} , Co^{2+} , and Fe^{2+} , in zinc and cadmium chalcogenides. Still, the exploration of the physics of these devices is incomplete. In this work, we analyze absorption spectra collected from Fe^{2+} ions in several binary, ternary, and quaternary host crystals at temperatures from a few degrees Kelvin to room temperature. We use the zero-phonon lines of the low-temperature spectra to calculate the value of the crystal field energy of Fe^{2+} ions in these hosts. We plot these crystal field energies with respect to the anion–cation distance of the host crystal and show that their crystal field strengths deviate somewhat from the trend predicted by crystal field theory. We use a model which we previously developed to describe the upper state lifetime of Fe^{2+} ions to predict the steady-state radiative efficiency of Fe:II–VI materials with respect to temperature. The impact of relative crystalline disorder on the output characteristics of lasers based on Cr:ZnS, Cr:ZnSe, Fe:ZnSe, and Fe:CdMnTe is explored. The effect of decreased long-range order of the host crystal is observed in the broadening of the absorption spectra of Fe^{2+} -doped ternary and quaternary alloys, the broadening of the spectral linewidth of continuous-wave Fe:II–VI lasers, and a reduction in the portion of the Cr:ZnSe emission spectrum accessible for modelocked lasing. This survey provides a richer picture of the tradespaces that can be leveraged when producing laser devices based on transition metal chalcogenides. © *The Authors. Published by SPIE under a Creative Commons Attribution 4.0 International License. Distribution or reproduction of this work in whole or in part requires full attribution of the original publication, including its DOI.* [DOI: [10.1117/1.OE.62.1.017101](https://doi.org/10.1117/1.OE.62.1.017101)]

Keywords: mid-infrared lasers; transition metals; spectroscopy; modeling.

Paper 20220839G received Jul. 27, 2022; accepted for publication Nov. 22, 2022; published online Jan. 11, 2023.

1 Background and Theory

In the previous two decades, vibronic lasers based on transition metal ions substitutionally incorporated into II–VI crystal hosts (most notably Cr:ZnSe and Fe:ZnSe) have become ubiquitous.^{1–6} Still, some of the fundamental interactions that influence the behavior of laser sources built from these materials are not widely appreciated. In this work, we draw attention to the sensitivity of the output characteristics of lasers made from these materials to the overall quality of the crystals used to construct them.

Iron and chromium ions take on the 2+ ionization state when they reside in cation sites within II–VI crystal matrices. Both ions have 25 energetically degenerate eigenstates in their 5D ground level. This degeneracy is lifted by the tetrahedrally symmetric Coulomb perturbation which these ions experience from their anionic nearest neighbors. This crystal field splitting of the ground state produces a 15-fold degenerate 5T_2 state and a 10-fold degenerate 5E state, which are further split by spin–orbit interactions. These levels are strongly coupled to the vibrational modes of the host crystal, giving rise to broad upper and lower state manifolds and optical cross-sections.

*Address all correspondence to Jonathan W. Evans, jonathan.evans.6@us.af.mil

The majority of this work is devoted to Fe^{2+} -based materials, which we have studied in more depth than those based on Cr^{2+} ions. Nevertheless, insights from Cr^{2+} -based materials are useful because of the complementary nature of the d^4 and d^6 electronic configurations. Henderson and Imbusch⁷ have shown that the crystal field energy Δ (sometimes expressed as $10Dq$) of the Fe^{2+} ion in a tetrahedral potential is expressed as

$$\Delta = \frac{K}{\pi\epsilon_0} \frac{Ze^2}{a^5} \langle r^4 \rangle_{3d}, \quad (1)$$

where K is a proportionality constant, $-Ze$ is the net charge of each nearest neighbor ion, a is the distance between the active ion and its nearest neighbors, and $\langle r^4 \rangle_{3d}$ represents an overlap integral of the electronic wave functions used in calculating the matrix elements of the crystal field Hamiltonian. These wave functions can be approximated via perturbation theory by adding successive refining terms to the familiar spherical harmonics of hydrogen-like atoms. Note that Eq (1) predicts that the crystal field energy of the Fe^{2+} ion in its host will be inversely proportional to its distance from its anionic neighbors raised to the fifth power. Thus, we expect that hosts which contain larger ions will have longer lasing wavelengths. This trend will be examined in Sec. 2.2. Also note that the cation–anion distance is called “ a ” by convention, which introduces an unfortunate ambiguity because this label does not refer to the lattice constant a of the host. We use this label throughout this work to refer to the former.

The Cr^{2+} ion and the Fe^{2+} ion can both be described using the same electronic and crystal field term symbols because they have complementary electron configurations. However, the Cr^{2+} ion is expected to have a crystal field energy of a larger magnitude and opposite sign.⁷ The effect of this sign change can be seen in Fig. 1 with the inversion of the 5E and 5T_2 levels in the energy level diagrams of the Cr^{2+} and Fe^{2+} ions. The relative magnitude of the field energy will be addressed in Sec. 2.1.2.

The eigenenergies of the Fe^{2+} ion are parameterized in three variables, such as Δ , λ , and σ , which each correspond uniquely to a subsequent quantum perturbation. Transitions between energy levels belonging to the 5E ground manifold and the 5T_2 upper manifold are optically active; however, not all possible transitions are allowed. Figure 2 shows the electric dipole allowed transitions between the states of each manifold identified by Slack et al.⁸ At cryogenic temperatures, some purely electronic transitions between energy levels can be resolved using a spectrometer as a series of zero-phonon lines (ZPLs) as shown in Sec. 2.1.1.

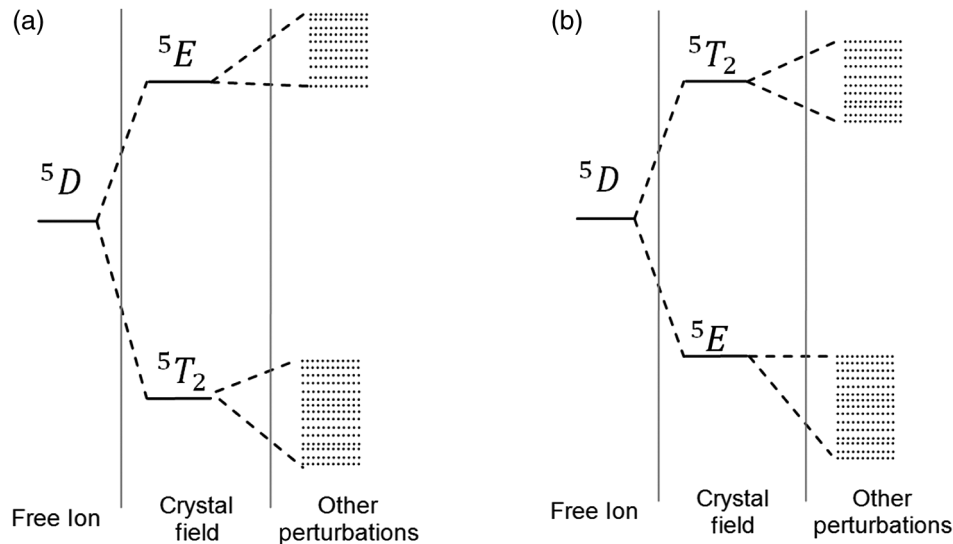


Fig. 1 The energy level diagrams for (a) Cr^{2+} and (b) Fe^{2+} ions in a tetrahedral potential.

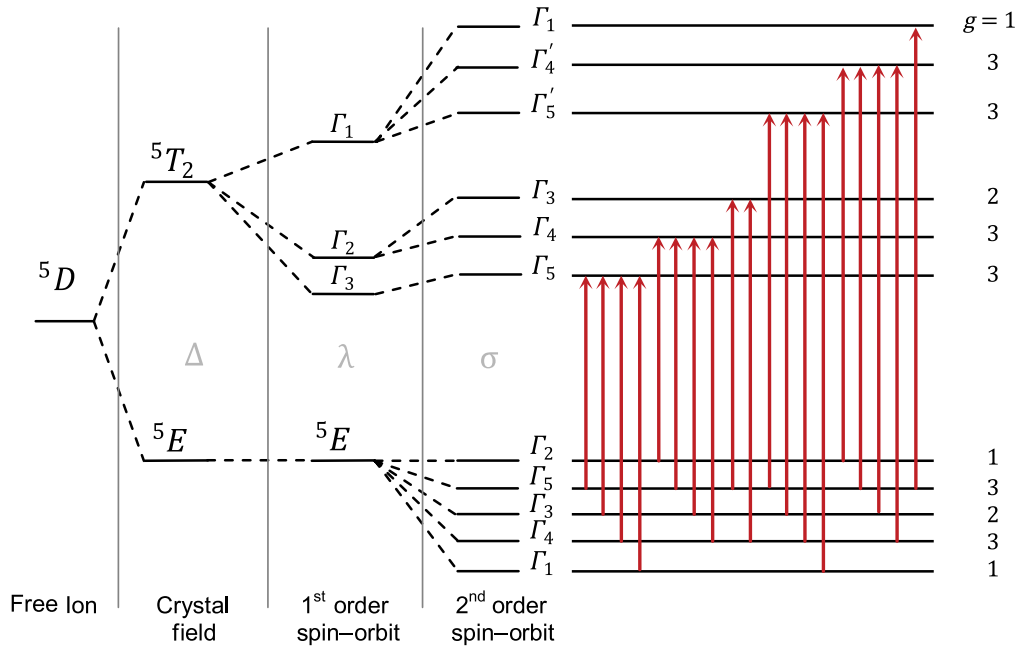


Fig. 2 The eigenenergies and allowed transitions (shown in absorption) of the Fe^{2+} ion in a tetrahedral potential.

At room temperature, these sharp features are broadened into a featureless band (see Sec. 3) due to phonon-assisted processes. Every Fe^{2+} ion in a single-site II–VI material (such as those with a zincblende structure) will be coupled to the vibration of its host in the same way, so this broadening process does not contribute to group formation. Consequently, we expect lasers based on such materials to be homogeneously broadened. At low temperatures, the strength of this coupling will depend primarily on the symmetry of the of the ground state level(s), thus the strength of this coupling is expected to be different for Cr^{2+} ions and Fe^{2+} ions.

Purely electronic transitions $\Gamma_m \leftrightarrow \Gamma_n$ between a 5T_2 level m and an 5E level n are characterized by an optical energy E_{mn} . The energies of the dominant transitions are

$$\begin{aligned}
 E_{55} &= \Psi + 6 \frac{\lambda^2}{\Delta} (1 + \sigma + \sigma^2), \\
 E_{53} &= \Psi + 12 \frac{\lambda^2}{\Delta} (1 + \sigma - 11\sigma^2), \\
 E_{54} &= \Psi + 18 \frac{\lambda^2}{\Delta} (1 - \sigma - 15\sigma^2), \\
 E_{51} &= \Psi + 24 \frac{\lambda^2}{\Delta} (1 - 2\sigma - 20\sigma^2),
 \end{aligned} \tag{2}$$

where

$$\Psi = \Delta + 3\lambda + \frac{18}{5} \frac{\lambda^2}{\Delta} \left(1 + \frac{63\sigma}{25} + \frac{4003\sigma^2}{625} \right), \tag{3}$$

Δ is the crystal field parameter, λ is the first-order spin–orbit parameter, and σ is the second-order spin–orbit parameter.⁹ In Sec. 2, we make use of this model to determine the crystal field energy of the Fe^{2+} ion in several chalcogenide host crystals from the ZPLs in their absorption spectra.

2 Trends in Transition Metal Chalcogenides

2.1 Low-Temperature Absorption Spectra

2.1.1 Fe:II–VI materials

The low-temperature absorption spectra of several binary Fe:Zn–VI samples are shown in Fig. 3. These spectra were acquired using a Nicolet 6700 FTIR spectrometer and a liquid helium cryostat from Advanced Research Systems (ARS) for temperature control. The cryostat featured uncoated CaF_2 windows and had a minimum achievable temperature of approximately 11 K. The Fe:ZnS ($N \approx 8 \times 10^{18} \text{ cm}^{-3}$) and Fe:ZnSe ($N \approx 1 \times 10^{17} \text{ cm}^{-3}$) samples were produced via post-growth thermal diffusion (PGTD) techniques by IPG Photonics. The Fe:ZnTe sample (target concentration of $1 \times 10^{19} \text{ cm}^{-3}$) was grown from melt by Brimrose Corporation using the Bridgman technique. The Fe:ZnO sample (concentration undetermined) was grown at the Sensors Directorate of the Air Force Research Laboratory (AFRL) using hydrothermal techniques.

The ZPLs of the Fe:ZnS and Fe:ZnSe absorption spectra are shown in Fig. 4. A similar series of four dominant lines is observed in each case. A few minor features are also observed which are not easily assigned to electric dipole allowed transitions. Notably, we observe these small extraneous features at energies slightly higher than the strongest ZPL in the Fe:ZnS[†] and Fe:ZnSe spectra at 2846 and 2748 cm^{-1} , respectively. Slack et al.⁸ observed a similar small sharp feature at 2966 cm^{-1} in Fe:ZnS at 2.7 K, which we do not observe in our spectrum. Their assignment of this feature to the $\Gamma_1 \rightarrow \Gamma_4$ transition is not consistent with other findings of their work, or with ours. It is possible that these features arise due to local axial stress in some samples, but we are not able to say so definitively.

In the analysis that follows, we assigned the dominant features to the transitions of Fig. 2 with least energy; for example, we assign $E_{51} = 2737 \text{ cm}^{-1}$, $E_{54} = 2721 \text{ cm}^{-1}$, $E_{53} = 2709 \text{ cm}^{-1}$, and $E_{55} = 2691 \text{ cm}^{-1}$ for Fe:ZnSe. The model for these energies involves three variables and is thus over-constrained. We used least squares error minimization techniques to find an inexact solution for the parameters of Eq. (2): $\Delta = 2937 \text{ cm}^{-1}$, $\lambda = -91.1 \text{ cm}^{-1}$, and $\sigma = 0.0291$. Note that the calculated values of the relative transition strengths and the energy degeneracies predict that the 2737 cm^{-1} line would be less intense than the 2721 cm^{-1} line, which is the opposite of

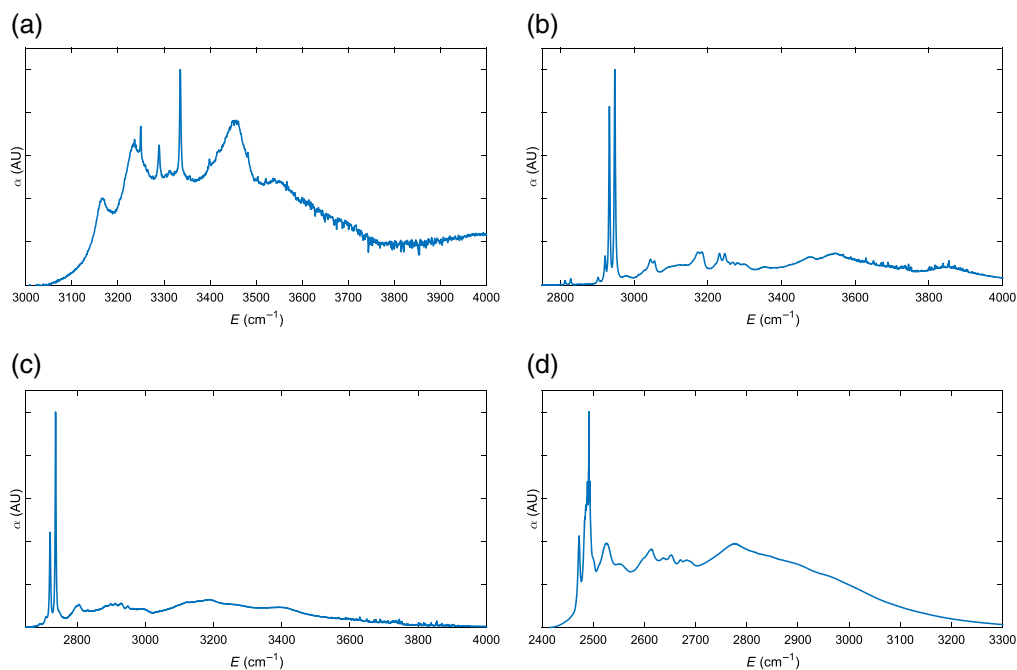


Fig. 3 The absorption spectra of several Fe:Zn–VI compounds at ~ 11 K: (a) Fe:ZnO, (b) Fe:ZnS, (c) Fe:ZnSe, and (d) Fe:ZnTe.

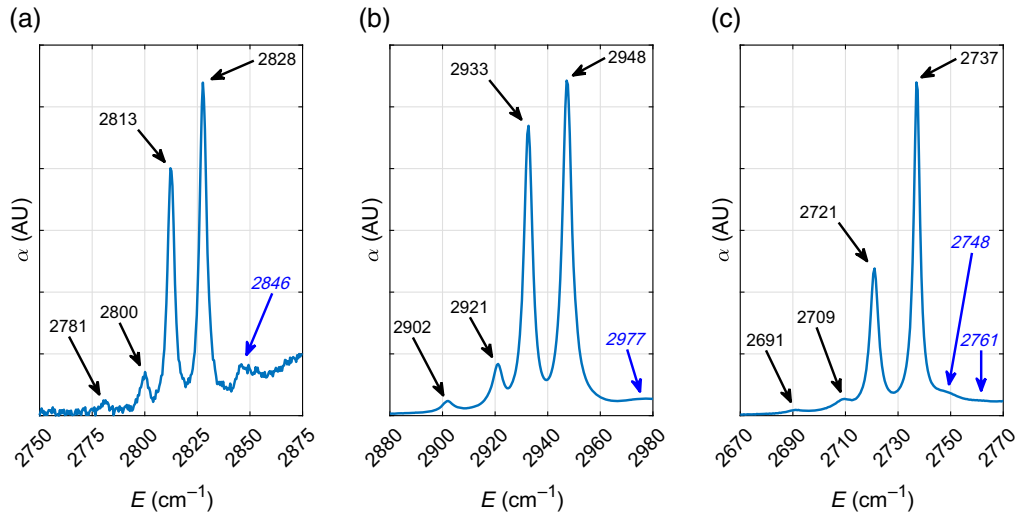


Fig. 4 The ZPLs of selected binary Fe:Zn–VI compounds from Fig. 3 shown in magnified detail: (a) Fe:ZnS[†], (b) Fe:ZnS, and (c) Fe:ZnSe. The dominant series are labeled in black, and extraneous features are labeled in blue italics.

what is observed.⁹ The Boltzmann statistics describing the distribution of population in the ground manifold are insufficient to account for this departure from the predicted intensities. However, this anomaly can be explained by the dynamic Jahn–Teller effect, which modifies the strength of the dipole moment of each transition.⁸ The interested reader can find a more detailed discussion of this departure in a previous work.¹⁰

The absorption spectra collected from the other Fe:Zn–VI samples were analyzed in this same way to determine host-specific values of Δ , λ , and σ . Furthermore, this analysis was also performed for Fe:Cd–VI materials using the absorption spectra from Fe:CdS,¹¹ Fe:CdSe,⁹ and Fe:CdTe⁹ obtained by sampling graphs published in the relevant literature (see Fig. 5). By performing this analysis for each of these Fe²⁺-doped compounds, we have assembled the data of Table 1.

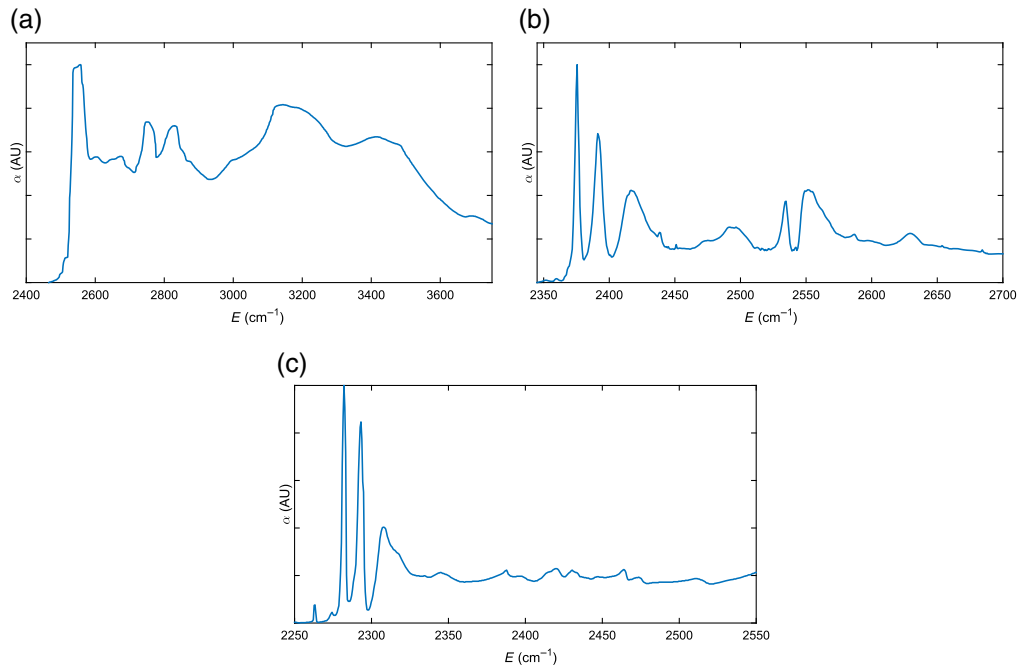


Fig. 5 The absorption spectra of several Fe:Cd–VI compounds at low temperatures as graphically sampled from other literature: (a) Fe:CdS ($T \approx K$),¹¹ (b) Fe:CdSe ($T \approx 2 K$),⁹ and (c) Fe:CdTe ($T \approx 5.7 K$).⁹

Table 1 Spectroscopic data and the corresponding values of Δ , λ , and σ for each Fe:II–VI sample.

Crystal	Fe ²⁺ concentration (cm ⁻³)	E_{51}	E_{54}	E_{53}	E_{55}	Δ (cm ⁻¹)	λ (cm ⁻¹)	σ	Cation–anion Distance (Å)
Fe:ZnO	—	3335	3288	3249	—	3620	-160	-0.0015	1.992 ¹²
Fe:ZnS	10 ¹⁷	2948	2933	2921	2902	3165	-98	0.041	2.274 ¹³
Fe:ZnS [†]	—	2828	2813	2800	2781	3040	-97	-0.039	2.312 ¹³
Fe:ZnSe	8 × 10 ¹⁸	2737	2721	2709	2691	2937	-91	0.029	2.459 ¹⁴
Fe:ZnTe	~10 ¹⁹	2492	2489	2487	—	2579	-33	-0.00026	2.598 ¹⁵
Fe:CdS	—	2556	2538	2511	2498	2751	-93	-0.099	2.502 ¹⁶
Fe:CdSe	5 × 10 ¹⁸	2391	2375	2362	2358	2563	-74	-0.15	2.634 ¹⁷
Fe:CdTe	5 × 10 ¹⁷	2293	2282	2274	2263	2441	-65	-0.014	2.804 ¹⁸

A similar table was generated by Mahoney et al. using an analysis derived from the measurement of magnetic susceptibility,¹⁹ and we note that their values for the crystal field strength Δ agree with ours to within a few percent with the notable exception of Fe:ZnO. Moreover, our estimates of the spin–orbit parameter λ agree with theirs to within an order of magnitude.

Unless otherwise specified, the energies of the dominant series of each Fe:II–VI compound are found by inspection of Figs. 3–5. The energies used for Fe:CdTe are those explicitly assigned by Udo et al.⁹ The second entry (†) for Fe:ZnS is the second of two line series from the Fe:ZnS polycrystal which have been analyzed. Both series are shown in Fig. 4. The secondary series is thought to arise from a small wurtzite component of the polycrystal, which has nearly tetrahedral site symmetry but which has a slightly larger average interionic distance than the zincblende component that gives rise to the primary series. The interionic distance a for each crystal in Table 1 was determined using the crystallographic information file corresponding to the reference indicated from the Inorganic Crystal Structure Database (ICSD) and Diamond crystal structure visualization software.

The selection of which absorption features to use to fit Δ , λ , and σ for the Fe:Cd–VI materials is complicated by interpretational ambiguities. Some of this ambiguity is introduced by the fact that these absorption spectra have been extracted from printed figures. Additional ambiguity is introduced by the possibility of further reductions in site symmetry. For example, Udo et al.⁹ assigned their Fe:CdSe spectra on the basis of C_{3V} symmetry due to asymmetric stretching of the lattice in the wurtzite structure of that crystal. Further, the features we have assigned as corresponding to the $\Gamma_1 \rightarrow \Gamma_5$ transition in CdSe and CdTe were attributed by Udo et al. to Fe²⁺ complexes. We hypothesize that they made these assignments because they expected the $\Gamma_1 \rightarrow \Gamma_5$ transition to correspond to the strongest feature in the absorption spectra (which we have assigned to $\Gamma_4 \rightarrow \Gamma_5$). This assumption holds for materials like Fe:ZnS and Fe:ZnSe, where Jahn–Teller effects modify the strength of individual transitions, but from Fig. 5(a) of our recent work,¹⁰ we see that models that include the oscillator strengths of these transitions in the absence of Jahn–Teller effects predict that the $\Gamma_4 \rightarrow \Gamma_5$ transition is stronger. Note, however, that the combined effect of all these ambiguities only changes the calculated value of Δ by about 10 cm⁻¹.

2.1.2 Cr:ZnSe

A similar analysis was attempted for Cr:ZnSe using the same experimental and mathematical methods. Fig. 6 shows the absorption spectrum of a Cr:ZnSe sample at 11 K. This sample of Cr:ZnSe was produced via PGTD by IPG Photonics; however, the Cr²⁺ concentration of this sample is not known. Small ZPLs were detected at this temperature and were observed to decrease in magnitude with increasing sample temperature as expected. In contrast to spectra collected from low-temperature Fe:II–VI materials, the spectrum of Cr:ZnSe is dominated by a vibronic sideband, as was observed by Vallin et al.²⁰ The crystal field energy of the Cr²⁺ ion in

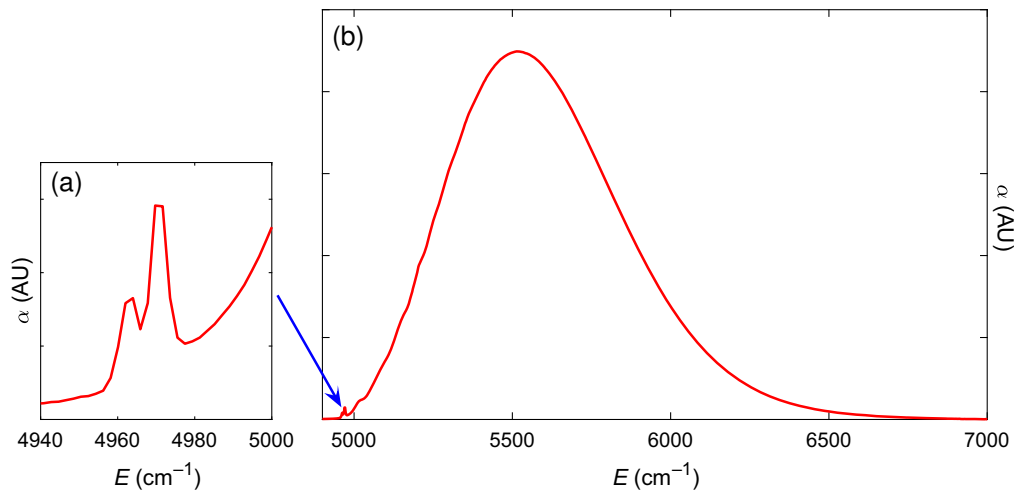


Fig. 6 The absorption spectrum of Cr:ZnSe at 11 K: (a) shows ZPLs at 4963 and 4971 cm^{-1} and (b) shows the vibronic sideband.

ZnSe can be determined approximately from Eq. (2). The reader will recall that, compared with the Fe^{2+} ion, the crystal field energy of the Cr^{2+} ion is opposite in sign so that the 5T_2 and 5E manifolds now contain the ground and excited states respectively. Consequently, the subscripts of the energies E_{mn} of the Fe^{2+} ion become E_{nm} for the Cr^{2+} ion. With only two ZPLs in the observed spectrum, the model of Eq. (2) is under-constrained. A naive fit for Δ and λ using $E_{15} = 4963 \text{ cm}^{-1}$ and $E_{45} = 4971 \text{ cm}^{-1}$ and assuming $\sigma = 0$ returns complex values for Δ and λ , which are undesirable. We further constrained the problem by requiring that Δ and λ be real and allowing σ to be a third fit parameter. Using this approach, we calculate $\Delta = -4967 \text{ cm}^{-1}$ (2013 nm), $\lambda = 4.347 \text{ cm}^{-1}$, and $\sigma = 3.098$. This value of Δ agrees well with the crystal field energies of 4600 and 4800 cm^{-1} calculated from Cr:ZnSe absorption spectra by Kaminska²¹ and Grebe,²² respectively. However, this solution implies the presence of ZPLs with $E_{35} = 4976 \text{ cm}^{-1}$ and $E_{55} = 4981 \text{ cm}^{-1}$, which are not observed in the Cr:ZnSe absorption spectrum. Other assignments give similar results, but also predict lines that are not observed. The absence of these lines suggests that our assignment of the ZPLs to the reciprocal transitions of the dominant series of Fe:ZnSe is incorrect, and that the Fe:II–VI model is not applicable to Cr:ZnSe without modification. The most promising candidate for such a modification would be the inclusion of a static Jahn–Teller distortion as noted by Vallin et al.²⁰

2.2 Crystal Field Energies of Fe^{2+} in Various Hosts

In Fig. 7, we plot the crystal field energy Δ of the Fe^{2+} ion in the II–VI compounds of Table 1 with respect to their cation–anion distances a . To compare this result to the predictions of theory, we fit a curve to the data using $\Delta = K'/a^b$. The best fit is obtained for $K' = 8362 \text{ \AA}^b \cdot \text{cm}^{-1}$ and $b = 1.204$. Colored bands in Fig. 7 represent the 90%, 95%, and 99% confidence intervals of the fit. From Eq. (1), we expect $b \approx 5$, so we see that the agreement between theory and experiment is less than compelling. We attribute this discrepancy to the limits of the model we have used, which approximates electrons as infinitesimal fixed point charges placed at the center of each host ion. Ligand field theory may provide some insight into this trend, but this consideration is beyond the scope of this work.

2.3 Minimization of Nonradiative Quenching in Fe:II–VI Gain Media

2.3.1 Estimating nonradiative quenching and radiative efficiency

Much of our previous work has focused on continuous-wave⁵ (CW) and Q-switched²³ lasers based on Fe:ZnSe. True CW lasing of Fe:ZnSe is prohibitively difficult at room temperature

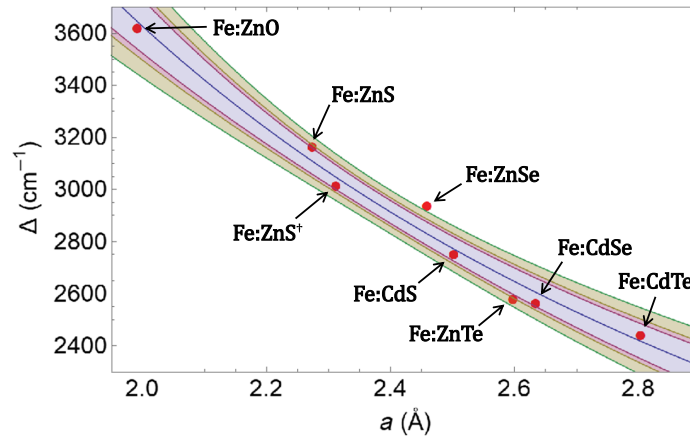


Fig. 7 The crystal field energy Δ of the Fe^{2+} ion in II–VI compounds with respect to the cation–anion distance a of the host. A similar graph in Baranowski et al.¹¹ plots the energy of the strongest ZPL with respect to a .

due to nonradiative processes which depopulate the 5T_2 manifold of the Fe^{2+} ion in ZnSe, and thus quench the radiative processes that drive lasing. This nonradiative quenching (NRQ) drives the radiative efficiency $<1\%$ at room temperature, so Fe:ZnSe has historically been cryogenically cooled to maintain efficient CW lasing.

In previous work,²⁴ we developed an analytical expression for the upper-state lifetime of the Fe^{2+} ion as a function of temperature. Ignoring energy transfer processes such as fluorescent reabsorption and nonradiative energy transfer, this expression becomes

$$\frac{1}{\tau_{\text{total}}} = \frac{1}{\tau_0} + \frac{A}{M^2 \sqrt{2\pi p}} \left(\frac{S e}{p} \right)^{p-2} \left(1 + \frac{1}{\exp\left(\frac{\Delta/p}{k_b T}\right) - 1} \right)^p, \quad (4)$$

where $\tau_0 \approx 48 \mu\text{s}$ is the radiative lifetime of the ion, k_b is Boltzmann’s constant, e is Euler’s constant, A is a coupling constant for the nonradiative term, M is an effective mass in atomic mass units (amu), S is the Huang–Rhys parameter, T is temperature, and Δ/p is the effective phonon energy $h\nu_{\text{eff}}$ required for p phonons to bridge the energy gap Δ between the energy levels involved in the optical transition. On average, the best fit of this expression to experimental values of the Fe:ZnSe lifetime is obtained for $A/M^2 = 10.4 \text{ ms}^{-1}$, $S = 5.45$, and $p = 16.1$. We model effective mass as $M_{\text{II-VI}} = \sqrt{M_{\text{II}} \cdot M_{\text{VI}}}$, so $M_{\text{ZnSe}} = \sqrt{65.4 \cdot 79 \text{ amu}^2} \approx 71.9 \text{ amu}$, which implies $A \approx 53.76 \mu\text{s}^{-1} \cdot \text{amu}^2$.

One goal of our investigation of various Fe:II–VI materials was to identify candidates, which are capable of CW lasing at or near room temperature. To assess the possibility of room-temperature CW lasing of the Fe^{2+} ion in hosts other than ZnSe, we used the value of A calculated above to evaluate Eq. (4) with respect to the effective mass M of each crystal in and the average number of phonons p involved in the quenching process. The radiative efficiency η is straightforwardly calculated from the ratio of the total lifetime of the ion to the radiative lifetime

$$\eta = \tau_{\text{total}}/\tau_0. \quad (5)$$

In Fig. 8, we plot η for Fe^{2+} -doped materials with respect to M and p for several values of temperature. The primary feature of these plots is an obvious “valley of death” in which NRQ dominates radiative relaxation, leading to poor lasing efficiency at values of $[M, p]$ within the valley.

A more detailed view of Fig. 8(b) is shown in Fig. 9 with values of $[M, p]$ corresponding to several binary II–VI hosts for Fe^{2+} superimposed. Note that, on the large- p side of the valley, radiative efficiency increases with respect to effective mass M and the phonon number p as expected. Note also that M and p are not independent in real materials; for a given value of the crystal field energy Δ , p increases with effective mass M . Consequently, most locations

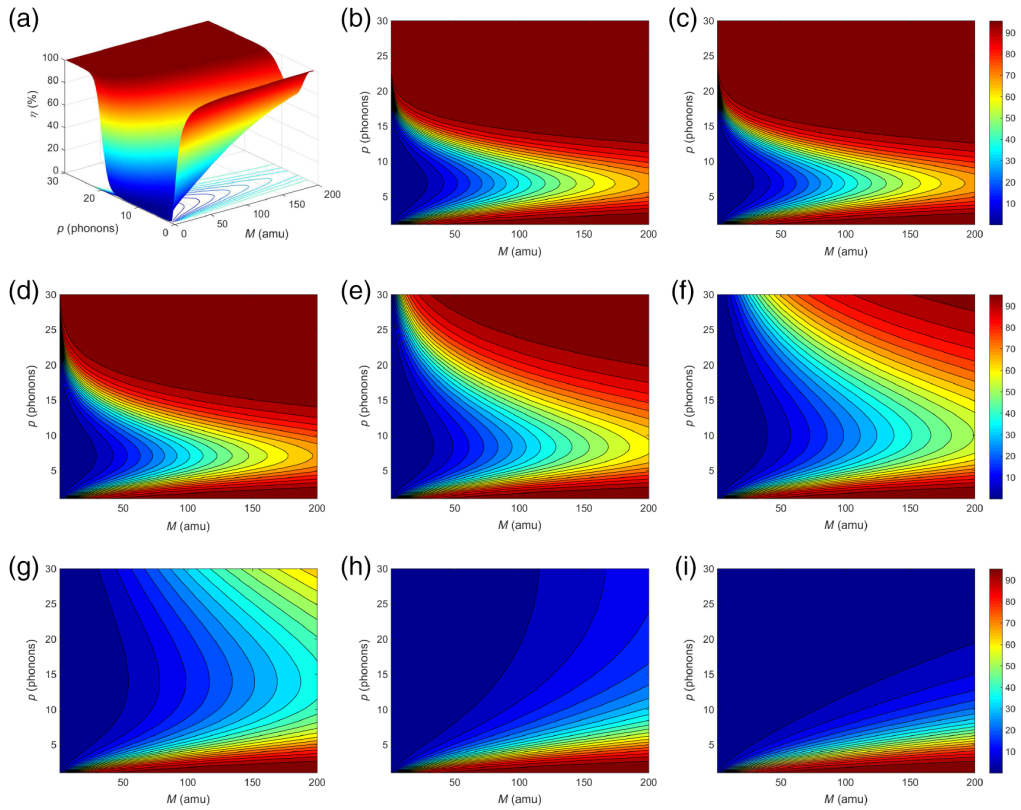


Fig. 8 The radiative efficiency surface at increasing values of temperature: (a) isometric $T \approx 0$ K, (b) $T \approx 0$ K, (c) $T \approx 50$ K, (d) $T \approx 100$ K, (e) $T \approx 150$ K, (f) $T \approx 175$ K, (g) $T \approx 200$ K, (h) $T \approx 225$ K, and (i) $T \approx 250$ K. The NRQ drastically reduces the radiative efficiency of the laser transition in Fe:II–VI materials with increasing temperature for $\rho > 7$.

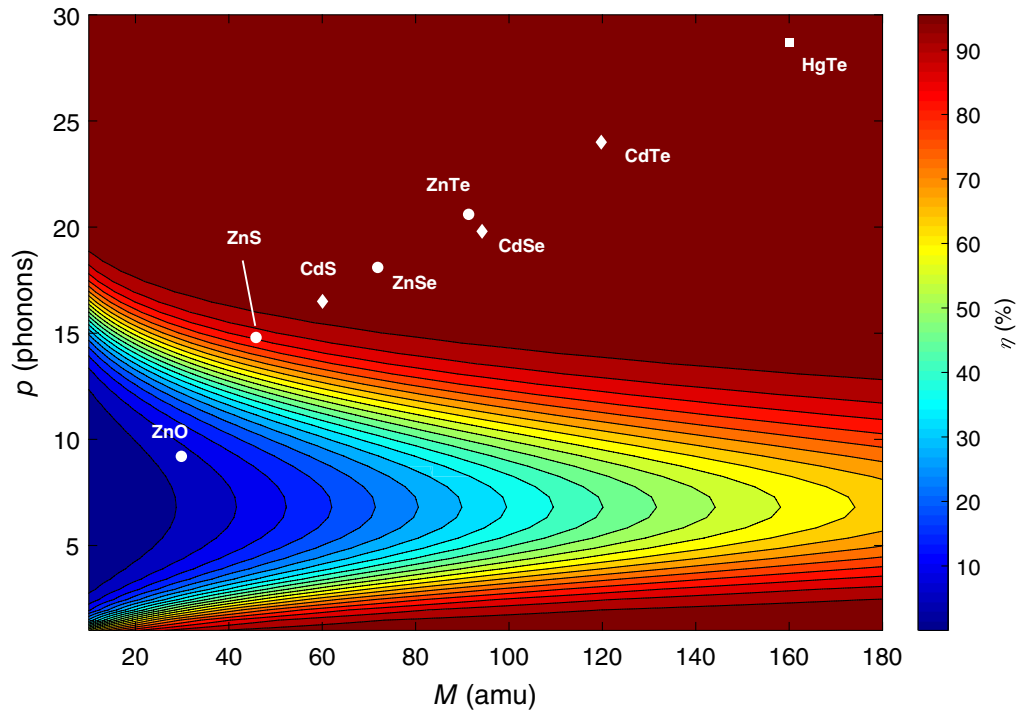


Fig. 9 The relative positions of several binary hosts on the $T \rightarrow 0$ K radiative efficiency surface. The approximate positions of II–VI alloy hosts can be inferred by interpolation.

on these surfaces do not correspond to real materials and M and p cannot be chosen arbitrarily. Nevertheless, the values of M and p can be chosen with some degree of flexibility by choosing ternary and quaternary II–VI alloys as hosts for Fe^{2+} ions.

It is interesting to note that on the low- p side of the valley, radiative efficiency does not vary strongly with temperature [compare 8(b) with 8(i)]. Theoretically, materials with $[M, p]$ in this region would not experience significant NRQ at elevated temperatures; however, no known Fe:II–VI material resides on the low- p side of the valley (see Fig. 9).

From the low-temperature plot of Fig. 9, one can clearly see that the ordered pair [71.9 amu, 16.1] (corresponding to ZnSe) resides near the edge of the strongly quenched region of the plot. As temperature increases, the gap widens and the radiative efficiency of Fe:ZnSe falls precipitously. It is clear by comparison of Figs. 8 and 9, that Fe^{2+} ions in each of these hosts will also experience NRQ at temperatures well below room-temperature. Thus, we expect that the radiative efficiency of these materials will fall monotonically with respect to increasing crystal temperature. Figure 10 shows the temperature-dependant radiative efficiency calculated from Eq. (5) for several binary hosts doped with Fe^{2+} ions.

Table 2 shows the values of M and p used in Fig. 9 and in the calculation of the radiative efficiencies shown in Fig. 10. The values of p were calculated by dividing the crystal field energy

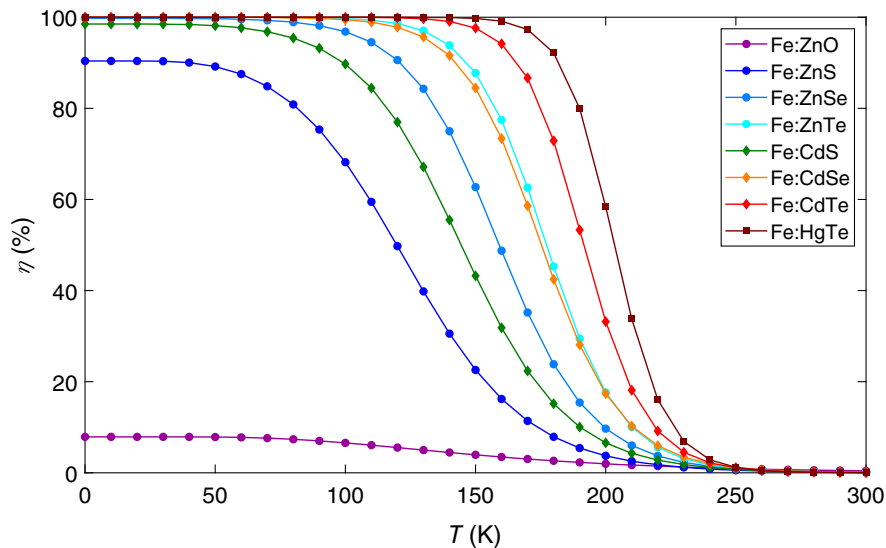


Fig. 10 The calculated radiative efficiency of Fe^{2+} ions in several binary hosts with respect to temperature.

Table 2 Effective masses and phonon numbers used for the calculation of radiative efficiency.

Crystal	M (amu)	E_{ph} (cm^{-1})	p
Fe:ZnO	29.8	393 ²⁵	9.2
Fe:ZnS	45.8	214 ²⁶	14.8
Fe:ZnSe	71.9	162 ²⁷	18.1
Fe:ZnTe	91.4	125 ²⁶	20.6
Fe:CdS	60.0	167 ²⁸	16.5
Fe:CdSe	94.2	129 ²⁹	19.8
Fe:CdTe	120	102 ²⁶	24.0
Fe:HgTe	160	85 ²⁶	28.5

of the Fe^{2+} ion in a given host by its characteristic phonon energy. The characteristic phonon energies were calculated as the centroid of the phonon density of states spectra taken from the literature cited in the table. The crystal field energy of the Fe^{2+} ion in HgTe was estimated to be 2426 cm^{-1} using the model of Fig. 7 with the interionic distance inferred to be 2.795 \AA from Skauli and Colin's model of the lattice parameter of HgCdTe.³⁰ It is worth noting that the band gap energy of $\text{Hg}_x\text{Cd}_{1-x}\text{Te}$ and the crystal field energy of the Fe^{2+} ion are equal at approximately $x = 0.69$. For larger values of x , the host would not be transparent to the radiation absorbed by the active ions and optical pumping of a laser based on such a gain medium would become infeasible. In this way, the $[M, p]$ tradespace of Fig. 9 is further restricted.

From Fig. 10, we see that the radiative efficiency of the laser transition in each of the Fe:II–VI materials becomes very low at room temperature. Thus, no candidate material is expected to lase continuously at room temperature. It is therefore not feasible to eliminate the need for aggressive cooling to achieve CW lasing in an Fe:II–VI laser by simply selecting a host material with large constituent ions. Furthermore, such a change would have spectral implications that may be undesirable, since using a material with a larger value of M would entail a red shift of the laser output wavelength (see Fig. 7). Nevertheless, NRQ does not preclude quasi-CW lasing for a relatively short time.

We also note from Fig. 10 that Fe:ZnS is significantly quenched, even at liquid nitrogen temperatures ($\sim 77 \text{ K}$), so we expect that CW lasing in Fe:ZnS would be characterized by higher pump thresholds and lower slope efficiencies than lasing in Fe:ZnSe under the same conditions. Interestingly, the unquenched lifetime of the Fe^{2+} ion is seen to increase from $<6 \mu\text{s}$ in Fe:ZnS³¹ to $48 \mu\text{s}$ in Fe:ZnSe²⁴ and to $>80 \mu\text{s}$ in Fe:CdMnTe,³² but these differences are not attributable the effect of NRQ alone. From Fig. 10, we would expect electronic relaxations in Fe:ZnO to be dominated by NRQ, even at temperatures approaching 0 K . To date, the authors are unaware of any demonstration of CW lasing in Fe:ZnO or Fe:ZnS. Nevertheless, the curves of Fig. 10 are seen to form a tradespace for managing NRQ in Fe:II–VI lasers.

2.3.2 Ternary and quaternary Fe:II–VI alloys

We have explored the $[M, p]$ tradespace for managing NRQ by experimental investigation of several II–VI alloys as hosts for Fe^{2+} ions including CdMnTe, CdMnMgTe, and HgCdTe. Samples were grown from melt by Brimrose Corporation using the Bridgman technique with a targeted Fe^{2+} concentration of $1 \times 10^{19} \text{ cm}^{-3}$. Two alloying fractions of Fe:CdMnTe were investigated: Fe:Cd_{0.85}Mn_{0.15}Te and Fe:Cd_{0.45}Mn_{0.55}Te. The alloying fraction of the Fe:CdMnMgTe sample was not known. The alloying fraction of the Fe:Hg _{x} Cd _{$1-x$} Te sample was approximately $x = 0.5$. The Fe:Cd_{0.85}Mn_{0.15}Te sample was later used to demonstrate a high-power quasi-CW laser at $5.2 \mu\text{m}$ (see Fig. 18). The interested reader can find separate publications dedicated to that work³² as well as to demonstrations of lasing in alloys such as Fe:ZnMgSe³³ and Fe:ZnMnTe.^{34,35}

The absorption spectra of these samples at 11 K and at room temperature are shown in Fig. 11. The reader will note that the bandgap energy of $\text{Hg}_x\text{Cd}_{1-x}\text{Te}$ approaches zero when

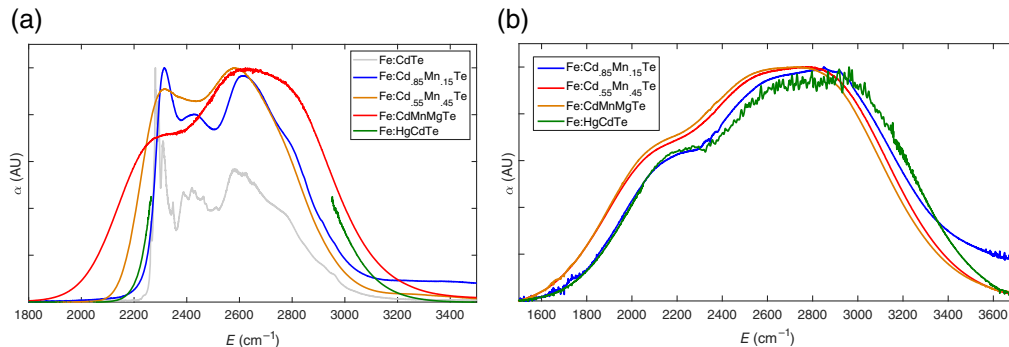


Fig. 11 The absorption spectra of Fe:Cd–VI alloys Fe:Cd_{0.85}Mn_{0.15}Te, Fe:Cd_{0.45}Mn_{0.55}Te, Fe:CdMnMgTe, and Fe:HgCdTe at (a) 11 K and (b) $\sim 295 \text{ K}$.

the group II alloying fraction exceeds 90% Hg. Using the formula of Hansen et al.,³⁶ we calculate the band gap energy of the sample to be $\sim 4550 \text{ cm}^{-1}$, which is about twice the energy of the optical transitions of Fe^{2+} ions within it. It can be seen in Figs. 11 and 14(d) that the HgCdTe host crystal was transparent in the region of the recorded absorption spectra.

In the ternary and quaternary systems, we expect that the long-range order of the crystal is not as regular as it is in binary systems. Therefore, there is no “canonical” site for the Fe^{2+} ion to inhabit. This multiplicity of possible environments leads to a smearing out of spectral features, thus no ZPLs are visible in the low temperature absorption spectra of the alloyed Fe^{2+} -doped materials. Nonetheless, each sample has a broad absorption band in the neighborhood of the Fe:CdTe spectrum.

Note that, despite some differences in the spectra of Fig. 11, the average energy of the absorption band does not change very much when the group II alloying fraction is varied. This result suggests that the primary effect on the crystal field energy is driven by the nearest neighbor Te^{2-} ion and that the next-to-nearest neighbor ions are too far away to have a major influence on the crystal field strength. This hypothesis is seemingly confirmed by the observation that the absorption spectra of Fe:ZnTe and Fe:CdTe as seen in Figs. 12(d) and 13, respectively, are nearly identical in shape other than a slight reduction in the overall energy of the later. The subtle changes to the spectra are hypothesized to arise from secondary effects which perturb the relative arrangement of the anionic nearest neighbors from site to site. Because binary crystals are not subject to these kinds of perturbations, we expect lasers based on binary transition metal doped II–VI compounds to be homogeneously broadened, whereas we expect lasers based on ternary or quaternary alloys doped with transition metal ions to be inhomogeneously broadened to some degree (see Sec. 4).

3 Fe:II–VI Temperature-Dependent Absorption Spectra

In addition to low-temperature absorption spectra, temperature-dependent absorption spectra were collected for several binary, ternary, and quaternary Fe:II–VI materials. The samples were cooled to the minimum temperature allowed by the helium cryostat and successive measurements were made as the temperature was increased. Stable temperatures were achieved using a closed-loop controller to drive a resistive heater. Samples were allowed to equilibrate for at least thirty minutes before an absorption measurement was collected.

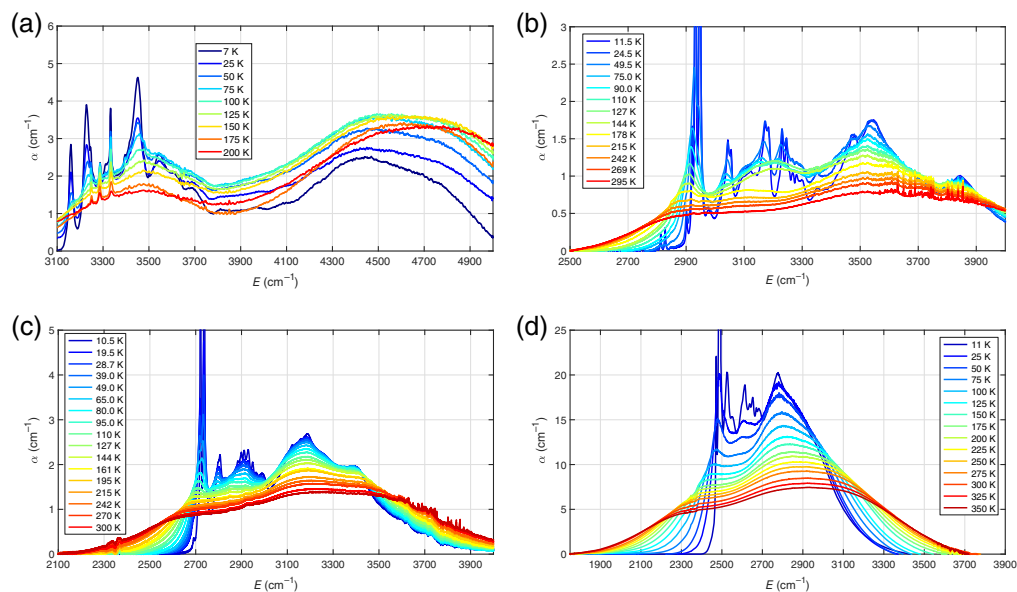


Fig. 12 The temperature-dependent absorption spectra of binary Fe:Zn–VI compounds: (a) Fe:ZnO, (b) Fe:ZnS, (c) Fe:ZnSe, and (d) Fe:ZnTe.

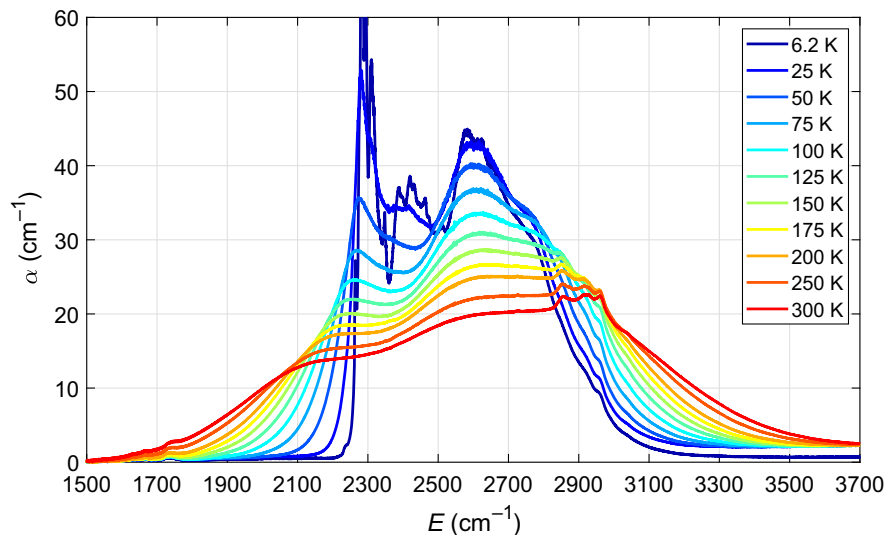


Fig. 13 The temperature-dependent absorption spectra of Fe:CdTe.

Figures 12 and 13 show the temperature-dependent absorption spectra from Fe:Zn–VI and Fe:CdTe, respectively. The absorption spectra of these binary Fe:II–VI materials are marked by ZPLs at low temperatures which gradually transition to featureless bands at elevated temperatures. In Figs. (b)–(d) of Fig. 12, the ZPLs extend beyond the upper limit of each graph to show more detail in the rest of the absorption features. Note that the data for the Fe:ZnO sample were collected using a cryostat from Cryo Industries of America (CIA), rather than the ARS cryostat used to collect the rest of the spectra shown in Fig. 12, so the minimum temperature is lower by a few degrees.

The spectra collected from the Fe:ZnO sample depart somewhat from the trends observed in spectra from the other Fe:Zn–VI samples. It is an open question whether this departure is due to crystal symmetry considerations, to factors unique to this particular sample, or to both. Though ZnO has a wurtzite crystal structure (rather than zincblende), the Zn sites are still approximately tetrahedrally coordinated by their surrounding anions. However, the slight axial stretch of the crystal lattice associated with wurtzite may distort the tetrahedral symmetry of those sites enough to produce energy level splittings and a deviation of the observed spectrum from the pattern observed in the zincblende hosts. This sample was unique among the samples we have included in this study in two ways: first, the sample was visibly occluded and showed some cracking, so the data collected may not be representative of a high-quality crystal of Fe:ZnO. The presence of multiple phases of ZnO within the sample has not been ruled out. Second, this sample was produced via hydrothermal growth techniques, rather than the PGTD, hot isostatic press (HIP), or melt techniques that are more common for Fe:II–VI materials, so contamination concerns cannot be ruled out even though the spectral features observed in Fig. 3(a) do not correspond to any expected from the mineralizers used in the growth process.

Despite this departure, the absorption spectrum of the Fe:ZnO sample exhibits some familiar trends with respect to temperature. Sharp features near 3300 cm^{-1} broaden into a nearly continuous band with increasing temperature. Curiously, the sharpest peaks at 3245 , 3287 , and 3332 cm^{-1} are still visible at 200 K , contrary to what we expect. The energies of these peaks shift slightly with changes in sample temperature. If we interpret these peaks as ZPLs (as we have in Sec. 2.1.1), the presence of strong absorption features at energies lower than these sharp features at low temperatures is difficult to explain, as they cannot be attributed to a phonon-assisted transition of the of the same type which give rise to the sharp features since $k_B T < 5\text{ cm}^{-1}$ at 7 K . This result, combined with the previously mentioned departure of our estimate of Δ for Fe:ZnO from that of Mahoney et al.,¹⁹ suggests that Eq. (2) is not a good model for the eigenenergies of the Fe^{2+} ion in ZnO.

Likewise, Fig. 13 shows the temperature-dependent absorption spectra of a sample of Fe:CdTe taken from 6.2 to 300 K . This sample of Fe:CdTe was produced using HIP

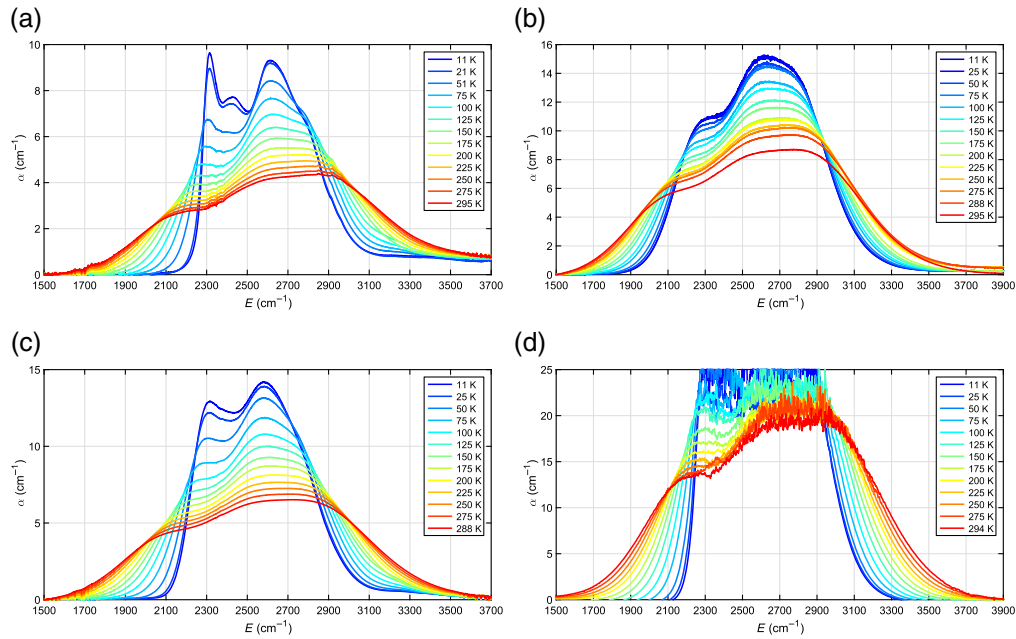


Fig. 14 The temperature-dependent absorption spectra of ternary and quaternary Fe:II-VI compounds: (a) Fe: Cd_{0.85}Mn_{0.15}Te, (b) Fe: Cd_{0.45}Mn_{0.55}Te, (c) Fe: CdMnMgTe, and (d) Fe: HgCdTe. Note, the total transmission of the Fe: HgCdTe sample was so low at $T < 100$ K, that the absorption measurements were saturated and dominated by noise, so we have shown only the nonsaturated portion of these spectra.

techniques³⁷ and the exact concentration of the Fe²⁺ ions was not measured, but we estimate that the average ionic concentration was $>10^{19}$ cm⁻³ based on the high optical density. The ZPLs are saturated in the measurement, but agree with the measurement of Udo et al.⁹ shown in Fig. 5(c). Like the Fe:ZnO sample, the Fe: CdTe sample was also cooled using the CIA cryostat. Like the temperature-dependent spectra of the Fe: Zn-VI samples, the Fe: CdTe spectra are marked by the evolution of clearly visible ZPLs at low temperature into smooth bands at elevated temperatures. Figure 14 shows the gradual evolution of the absorption spectra of the ternary and quaternary Fe:II-VI alloys of Sec. 2 with increasing temperature.

When taking absorption measurements, the Nicolet 6700 FTIR performs a background correction to compensate for the absorption of light by atmospheric gases in the laboratory environment. The concentration of atmospheric gasses in the laboratory clearly changed somewhat over the extended period of time that was required to make these measurements as features that are attributable to a changing background concentration of H₂O (~ 3700 cm⁻¹) and CO₂ (~ 2350 cm⁻¹) are clearly seen in the spectra at higher temperatures. Furthermore, there is some evidence of slight contamination in some of the spectra as evidenced by the presence of absorption features that are attributable to C-H stretching vibrations of the CH₂ (2853 and 2918 cm⁻¹) and CH₃ (2960 cm⁻¹) groups. These lines are most clearly seen in Fig. 13. The spectra were compensated for temperature-dependent Fresnel losses by subtracting a baseline loss calculated by assuming the loss at low energies is zero. This does approach does not consider the spectral dependence of the Fresnel loss. The effect of ignoring the spectral dependence of these losses can be seen in some of the absorption spectra as an increase in the baseline loss at higher energies, most notably in Fig. 14(a).

4 Crystal Effects on Emission Linewidth

Finally, we turn our attention to recent findings that link crystal quality to laser linewidth. Historically, Cr:ZnSe and Fe:ZnSe lasers demonstrated in our lab and reported in the literature have exhibited broad-band output spectra^{3,5,38-40} like those shown in Fig. 15.

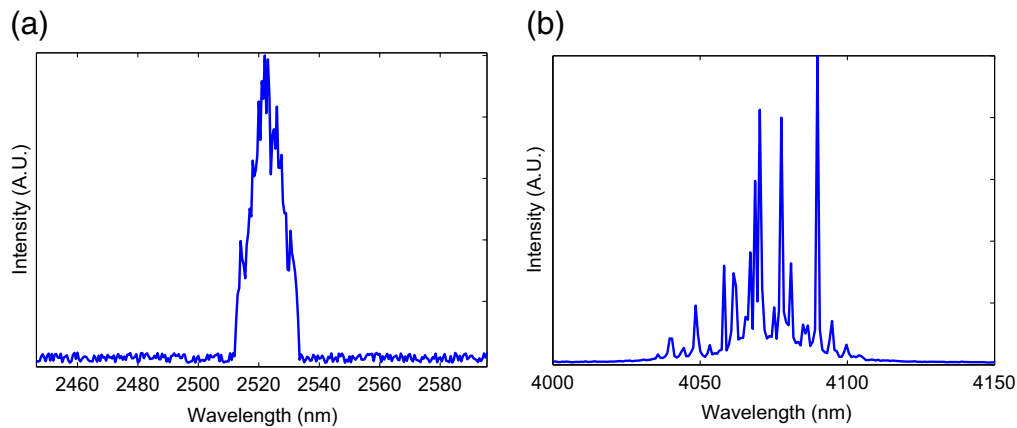


Fig. 15 Broadband output spectra of CW: (a) Cr:ZnSe and (b) Fe:ZnSe lasers.

The description of tetrahedrally coordinated transition metals ions provided by group theory suggests no broadening mechanism that would lead to inhomogeneous broadening of corresponding lasers. So, either the spectra seen in Fig. 15 represent the homogeneously broadened linewidth of such lasers or the active ions experience a multiplicity of environmental perturbations, most plausibly from the occupation of group II sites in lattices that are significantly distorted from tetrahedral symmetry in a variety of ways. Several recent observations suggest the latter case.

1. We have previously demonstrated a waveguide microchip laser made by writing the waveguide into Cr:ZnSe using ultrafast laser inscription to locally modify the refractive index of the sample.⁴¹ The modification of the laser material had the unintended consequence of producing a laser device with an output linewidth of only 0.7 nm (see Fig. 16), as compared with the ~ 20 nm linewidth of Fig. 15.
2. We have previously demonstrated a Cr:ZnSe laser based on a crystal produced using exclusively HIP techniques.³⁷ Figure 17(a) shows the output spectrum of this laser, which is seen to collapse to a subnanometer linewidth.
3. In another work,⁴² we used HIP techniques to modify Fe:ZnSe laser samples originally prepared by PGTD. In Fig. 17(b), the output linewidth of a CW Fe:ZnSe laser is shown before and after the laser crystal was treated using HIP techniques. As in Cr:ZnSe, the Fe:ZnSe output linewidth was less than 1 nm after HIP treatment.

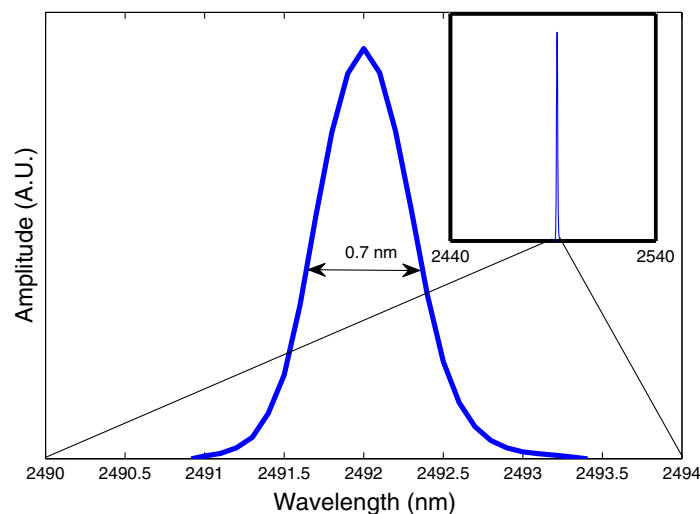


Fig. 16 The output spectrum of a gain-switched Cr:ZnSe microchip waveguide laser after modification by ultrafast laser inscription.

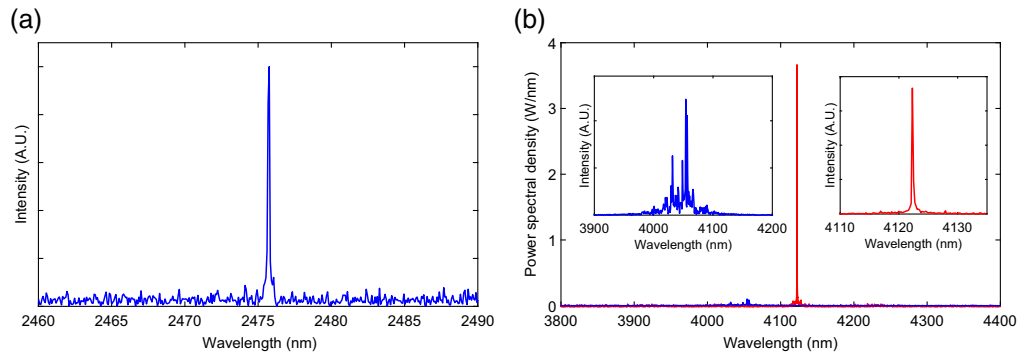


Fig. 17 The output spectra of (a) a CW laser based on Cr:ZnSe made by HIP techniques and (b) a CW laser based on Fe:ZnSe originally made by PGTD techniques before (blue) and after (red) HIP treatment.

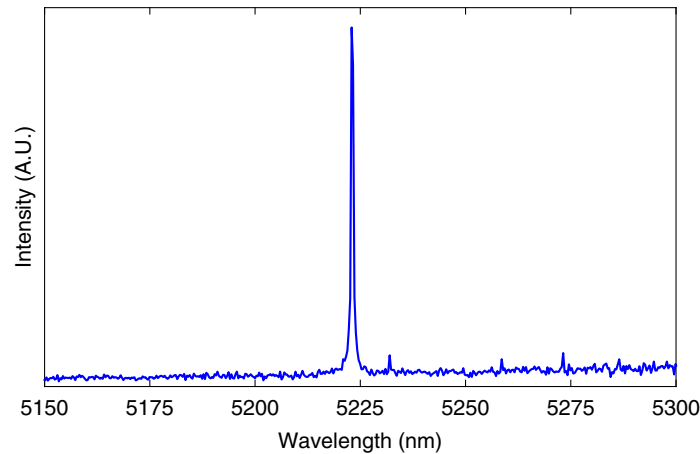


Fig. 18 The output spectrum of a quasi-CW laser based on Fe:CdMnTe grown from melt.

4. We have previously demonstrated a powerful Fe:CdMnTe laser.³² The laser was constructed using a sample that was grown from melt using the Bridgman technique, rather than produced by PGTD. Despite the expectation of some inhomogeneous broadening due to a multiplicity of possible arrangements for the nearest neighbors of the Fe²⁺ ion, the laser had an output linewidth of approximately 1 nm (see Fig. 18), which was the resolution limit of the instrument used to measure it.

These results in both Cr²⁺- and Fe²⁺-doped II–VI materials show that the native linewidth of lasers based on these ions can be very narrow, as is typical in rare-earth lasers systems. Consequently, we hypothesize that historically broadband output spectra from such lasers are due to inhomogeneous broadening that arises from randomly distributed distortions of the site symmetry of the active ion away from purely tetrahedral symmetry. Fundamentally, we see that the spectral properties of transition metal lasers are highly dependent on the local environment which they inhabit. This sensitivity arises from the fact that the electronic transitions in such lasers involve *d*-orbitals, which are not well shielded from external perturbations in the way that the *f*-orbitals of rare earth ions are shielded by their fully filled exterior electronic shells.⁴³

4.1 Implications for Modelocking

Ultrafast pulses generated in the mid-IR spectral region have been of considerable scientific interest for some time. Recent work has shown excellent results in the 2 to 3 μm region from modelocked sources based on Cr:ZnS^{44,45} and Cr:ZnSe⁴⁶ with few-cycle pulses produced by Kerr lens modelocking. In the 4 to 5 μm region, hybrid sources combining ultrafast sources with Fe:ZnSe amplifiers^{47,48} and directly modelocked Fe:ZnSe laser sources⁴⁹ have been

demonstrated recently. These sources have the potential to have all the scientific utility of the Ti:Sapphire laser in this unique part of the optical spectrum, and our findings have implications for the self-starting threshold of modelocked sources based on Cr:II–VI and Fe:II–VI gain media.

The transform-limited pulsewidth of a modelocked pulse is typically smaller for inhomogeneously broadened gain media than for homogeneously broadened media, leading to higher values of peak power. Thus, Nd³⁺-doped glasses are often preferred over Nd³⁺-doped crystals for commercial modelocked sources. However, the work of Zehetner et al. has shown the self-starting threshold of CW pumped modelocked sources based on homogeneously broadened Nd³⁺-doped phosphate glass to be considerably lower than in inhomogeneously broadened Nd³⁺-doped silicate glass.⁵⁰ We point out that the inhomogeneous fluorescence bandwidth of disordered transition metal chalcogenides is not measurably broader than the homogeneously broadened emission of their well-ordered counterparts. Thus, it is thus plausible that the use of well-ordered materials of this type to generate ultrashort pulses will benefit from absence of inhomogeneous broadening without significantly affecting the transform limit of pulsewidth. Thus, pulse stability and threshold considerations may influence a designer's choice in specifying the crystal quality of transition metal chalcogenide gain media in the modelocked regime.

Finally, we also note that our recent collaboration with Herriot–Watt University and Politecnico di Milano has shown the shortest ultrafast pulse ever generated in Cr:ZnSe (34 fs) using material produced using HIP techniques.⁵¹ The improved stability of the modelocking and increased lockable bandwidth is attributed to the use of homogeneously broadened media. A more complete discussion of lockable bandwidth in inhomogeneously broadened lasers is found in Yan and Han.⁵²

5 Conclusion

We have discussed the role of crystal field theory in understanding the behavior of lasers based on Cr²⁺ and Fe²⁺ ions doped into II–VI hosts. We showed the absorption spectra of several Fe:II–VI materials and have reported values of the crystal field energy of the Fe²⁺ ion calculated from these spectra. We apply our model for NRQ of the fluorescence of Fe²⁺ ions to find temperature-dependent radiative efficiencies for these materials. Thus, we show that crystal field engineering is insufficient to produce room temperature CW lasing from Fe:II–VI materials. We show that narrow linewidth operation of lasers based on Cr²⁺ and Fe²⁺ ions suggests that historical results featuring broad emission linewidths are probably due to inhomogeneous broadening that arises from local distortions of the site symmetry of the active ion in samples fabricated by PGTD. Finally, well-ordered homogeneously broadened transition metal chalcogenides are shown to outperform their disordered inhomogeneously broadened counterparts in modelocking applications.

Acknowledgments

The authors thank the Sensors Directorate of AFRL for funding this effort. We also thank Dr. J. Matthew Mann for technical assistance with obtaining the crystal structure data. We also thank Drs. Sudhir Trivedi and Glen Perram for technical discussions. We also thank Pamela Evans for proofreading this manuscript. An earlier version of this manuscript was published in part in the proceedings of the LASE conference at Photonics West in 2020.⁵³ Some structural changes have been made to the manuscript as well as its figures and tables for the purpose of clarity. We have made small corrections to some of our calculations, and we have more thoroughly cited the literature relevant to our findings. Notably, we have added Figs. 12(a) and 13, which show the temperature-dependent absorption spectra of Fe:ZnO and Fe:CdTe, respectively.

References

1. S. B. Mirov et al., “Frontiers of mid-IR lasers based on transition metal doped chalcogenides,” *IEEE J. Sel. Top. Quantum Electron.* **24**, 1–29 (2018).

2. M. P. Frolov et al., “2 mJ room temperature Fe: CdTe laser tunable from 5.1 to 6.3 μm ,” *Opt. Lett.* **44**, 5453–5456 (2019).
3. M. Doroshenko et al., “Tunable mid-infrared laser properties of $\text{Cr}^{2+}:\text{ZnMgSe}$ and $\text{Fe}^{2+}:\text{ZnSe}$ crystals,” *Laser Phys. Lett.* **7**, 38–45 (2010).
4. H. Jelínková et al., “ $\text{Fe}^{2+}:\text{Cd}_{1-x}\text{Mn}_x\text{Te}$ ($x = 0.1\text{--}0.76$) laser generating at 5.5–6 μm at room temperature,” in *CLEO Europe OSA Technical Digest*, Optical Society of America, p. ca_p_18 (2019).
5. J. W. Evans, P. A. Berry, and K. L. Schepler, “840 mW continuous-wave Fe: ZnSe laser operating at 4140 nm,” *Opt. Lett.* **37**, 5021–5023 (2012).
6. E. J. Turner et al., “Double-pass Co: CdTe mid-infrared laser amplifier,” *Opt. Mater. Express* **8**, 2948–2953 (2018).
7. B. Henderson and G. F. Imbusch, *Optical Spectroscopy of Inorganic Solids*, Monographs on the Physics and Chemistry of Materials, Clarendon Press, Oxford (1989).
8. G. A. Slack, F. S. Ham, and R. M. Chrenko, “Optical absorption of tetrahedral Fe^{2+} ($3d_6$) in cubic ZnS, CdTe, and MgAl_2O_4 ,” *Phys. Rev.* **152**, 376–402 (1966).
9. M. K. Udo et al., “Electronic excitations of substitutional transition-metal ions in II–VI semiconductors: CdTe: Fe^{2+} and CdSe: Fe^{2+} ,” *Phys. Rev. B* **46**, 7459–7468 (1992).
10. J. W. Evans et al., “Optical spectroscopy and modeling of Fe^{2+} ions in zinc selenide,” *J. Lumin.* **188**, 541–550 (2017).
11. J. M. Baranowski, J. W. Allen, and G. L. Pearson, “Crystal-field spectra of $3d_n$ impurities in II–VI and III–V compound semiconductors,” *Phys. Rev.* **160**, 627–632 (1967).
12. Y. Kim et al., “Optical and electronic properties of post-annealed ZnO: Al thin films,” *Appl. Phys. Lett.* **96**(17), 171902 (2010).
13. M. El-Hagary et al., “Composition, annealing and thickness dependence of structural and optical studies on $\text{Zn}_{1-x}\text{Mn}_x\text{S}$ nanocrystalline semiconductor thin films,” *Mater. Chem. Phys.* **132**(2), 581–590 (2012).
14. J. Sharma and S. Tripathi, “Effect of deposition pressure on structural, optical and electrical properties of zinc selenide thin films,” *Phys. B Condens. Matter* **406**(9), 1757–1762 (2011).
15. M. Emam-Ismael et al., “Microstructure and optical studies of electron beam evaporated $\text{ZnSe}_{1-x}\text{Te}_x$ nanocrystalline thin films,” *J. Alloys Compd.* **532**, 16–24 (2012).
16. M. Barote et al., “Optical and electrical characterization of chemical bath deposited Cd–Pb–S thin films,” *Thin Solid Films* **526**, 97–102 (2012).
17. H. Sowa, “The high-pressure behaviour of CdSe up to 3 GPa and the orientation relations between its wurtzite- and NaCl-type modifications,” *Solid State Sci.* **7**(11), 1384–1389 (2005).
18. C. Campos et al., “Influence of minor oxidation of the precursor powders to form nanocrystalline CdTe by mechanical alloying,” *J. Alloys Compd.* **466**(1), 80–86 (2008).
19. J. P. Mahoney et al., “Determination of the spin–orbit and trigonal-field splittings of the ^5E state of Fe^{2+} in ZnO, ZnS, CdS, ZnSe, CdSe, ZnTe, and CdTe crystals by magnetic susceptibilities,” *J. Chem. Phys.* **53**(11), 4286–4290 (1970).
20. J. T. Vallin et al., “Infrared absorption in some II–VI compounds doped with Cr,” *Phys. Rev. B* **2**, 4313–4333 (1970).
21. M. Kaminska et al., “Absorption and luminescence of Cr^{2+} (d_4) in II–VI compounds,” *J. Phys. C Solid State Phys.* **12**, 2197–2214 (1979).
22. G. Grebe, G. Roussos, and H. J. Schulz, “ Cr^{2+} excitation levels in ZnSe and ZnS,” *J. Phys. C Solid State Phys.* **9**, 4511–4516 (1976).
23. J. Evans, P. Berry, and K. Schepler, “A passively Q-switched, CW-pumped Fe: ZnSe laser,” *IEEE J. Quantum Electron.* **50**(3), 204–209 (2014).
24. J. W. Evans et al., “Re-absorption and nonradiative energy transfer in vibronic laser gain media,” *Opt. Eng.* **60**(5), 056103 (2021).
25. D. Raymand et al., “Investigation of vibrational modes and phonon density of states in ZnO quantum dots,” *J. Phys. Chem. C* **116**(12), 6893–6901 (2012).
26. B. Rajput and D. Browne, “Lattice dynamics of II–VI materials using the adiabatic bond-charge model,” *Phys. Rev. B* **53**(14), 9052 (1996).
27. B. Hennion et al., “Normal modes of vibrations in ZnSe,” *Phys. Lett. A* **36**(5), 376–378 (1971).

28. J. Camacho and A. Cantarero, "Lattice dynamics in Wurtzite semiconductors: the bond charge model of CdS," *Phys. Status Solidi b* **215**(1), 181–187 (1999).
29. M. Mohr and C. Thomsen, "Phonons in bulk CdSe and CdSe nanowires," *Nanotechnology* **20**, 115707 (2009).
30. T. Skauli and T. Colin, "Accurate determination of the lattice constant of molecular beam epitaxial CdHgTe," *J. Cryst. Growth* **222**(4), 719–725 (2001).
31. N. Myoung et al., "Temperature and concentration quenching of mid-IR photoluminescence in iron doped ZnSe and ZnS laser crystals," *J. Lumin.* **132**(3), 600–606 (2012).
32. J. W. Evans et al., "Demonstration and power scaling of an Fe:CdMnTe laser at 5.2 microns," *Opt. Mater. Express* **7**, 860–867 (2017).
33. M. E. Doroshenko et al., "Spectroscopic and laser properties of bulk iron doped zinc magnesium selenide Fe:ZnMgSe generating at 4.5–5.1 μm ," *Opt. Express* **24**, 19824–19834 (2016).
34. M. E. Doroshenko et al., "Comparison of novel $\text{Fe}^{2+}:\text{Zn}_{1-x}\text{Mn}_x\text{Te}$ ($x\approx 0.3$) laser crystal operating near 5 μm at 78 K with other known Mn co-doped $\text{A}^{\text{II}}\text{-B}^{\text{VI}}$ solid solutions," *Opt. Mater.* **108**, 110392 (2020).
35. H. Jelínková et al., "Fe:ZnMnTe laser generating around 5 μm at 78 K," *Proc. SPIE* **11259**, 1125923 (2020).
36. G. L. Hansen, J. L. Schmit, and T. N. Casselman, "Energy gap versus alloy composition and temperature in $\text{Hg}_{1-x}\text{Cd}_x\text{Te}$," *J. Appl. Phys.* **53**(10), 7099–7101 (1982).
37. R. W. Stites et al., "Hot isostatic pressing of transition metal ions into chalcogenide laser host crystals," *Opt. Mater. Express* **6**, 3339–3353 (2016).
38. S. McDaniel et al., "Cr:ZnSe laser incorporating anti-reflection microstructures exhibiting low-loss, damage-resistant lasing at near quantum limit efficiency," *Opt. Mater. Express* **4**, 2225–2232 (2014).
39. A. V. Pushkin et al., "Compact, highly efficient, 2.1-W continuous-wave mid-infrared Fe:ZnSe coherent source, pumped by an Er:ZBLAN fiber laser," *Opt. Lett.* **43**, 5941–5944 (2018).
40. G. Renz et al., "Cr:ZnSe thin disk CW laser," *Proc. SPIE* **8599**, 85991M (2013).
41. S. A. McDaniel et al., "Gain-switched operation of ultrafast laser inscribed waveguides in Cr:ZnSe," *Proc. SPIE* **9342**, 93420E (2015).
42. J. W. Evans, R. W. Stites, and T. R. Harris, "Increasing the performance of an Fe:ZnSe laser using a hot isostatic press," *Opt. Mater. Express* **7**, 4296–4303 (2017).
43. R. E. Watson and A. J. Freeman, "Shielding and distortion of rare-earth crystal-field spectra," *Phys. Rev.* **133**, A1571–A1584 (1964).
44. D. Okazaki et al., "Self-starting mode-locked Cr:ZnS laser using single-walled carbon nanotubes with resonant absorption at 2.4 μm ," *Opt. Lett.* **44**, 1750–1753 (2019).
45. S. Vasilyev et al., "Middle-IR frequency comb based on Cr:ZnS laser," *Opt. Express* **27**, 35079–35087 (2019).
46. S. Vasilyev et al., "1.5-mJ Cr:ZnSe chirped pulse amplifier seeded by a Kerr-lens mode-locked Cr:ZnS oscillator," in *Laser Congr.*, Optical Society of America, p. ATu4A.4 (2019).
47. F. V. Potemkin et al., "Gigawatt mid-IR (4 – 5 μm) femtosecond hybrid $\text{Fe}^{2+}:\text{ZnSe}$ laser system," *Proc. SPIE* **10238**, 102380L (2017).
48. E. Migal et al., "3.5-mJ 150-fs Fe:ZnSe hybrid mid-IR femtosecond laser at 4.4 μm for driving extreme nonlinear optics," *Opt. Lett.* **44**, 2550–2553 (2019).
49. A. V. Pushkin et al., "Femtosecond graphene mode-locked Fe:ZnSe laser at 4.4 μm ," *Opt. Lett.* **45**, 738–741 (2020).
50. J. Zehetner, C. Spielmann, and F. Krausz, "Passive mode locking of homogeneously and inhomogeneously broadened lasers," *Opt. Lett.* **17**, 871–873 (1992).
51. Y. Wang et al., "Hot-isostatic-pressed Cr:ZnSe ultrafast laser at 2.4 μm ," *Opt. Laser Technol.* **154**, 108300 (2022).
52. L. Yan and S. Han, "Passive mode locking of inhomogeneously broadened lasers," *J. Opt. Soc. Am. B* **24**, 2108–2118 (2007).
53. J. W. Evans et al., "Crystal host engineering for transition metal lasers," *Proc. SPIE* **11259**, 112590C (2020).

Jonathan W. Evans received his MS degree in electro-optics from the University of Dayton and a PhD in optical sciences and engineering from Air Force Institute of Technology. Currently, he is working as an assistant professor of engineering physics at the Air Force Institute of Technology and was formerly a research physicist at the AFRL, both at Wright–Patterson Air Force Base. His research interests include transition metal lasers, nonlinear parametric conversion, and laser spectroscopy. He is a member of SPIE and a senior member of Optica.

Sean A. McDaniel received his BS degree in physics from Otterbein College and MS and PhD degrees from the University of Dayton. He has worked in the Optoelectronic Technology Branch of the Air Force Research Laboratory at Wright–Patterson Air Force Base since 2010, first as an optical engineer for Leidos and then as a research physicist for the Sensors Directorate. His research interests include solid state lasers and integrated photonics.

Ronald W. Stites received his BS and MS degrees from Miami University before completing his PhD at the Pennsylvania State University studying atomic, molecular, and optical physics. He is working as a research physicist at the Air Force Research Laboratory with a background in optoelectronic and laser technology.

Patrick A. Berry received his BS degree in chemistry and physics from the University of Wisconsin-La Crosse in 2003 and his MS and PhD degrees in electro-optics from the University of Dayton in 2005 and 2010. Since 2003, he has worked in laser source and infrared counter-measures development for the Sensors Directorate of the US Air Force Research Laboratory. His research interests include high-power versatile laser sources for the mid-infrared region.

Gary Cook received his PhD in lasers and nonlinear optics from the University of Hull in the United Kingdom in 1998. He has worked in the optoelectronic technology branch of the Air Force Research Laboratory (AFRL), Sensors Directorate at Wright–Patterson Air Force Base since 2012. Prior to that, he worked as a laser and nonlinear optics research scientist in the United Kingdom before moving to the Materials and Manufacturing Directorate at AFRL in 2004. His research interests include lasers and nonlinear optics. He is a fellow of the Institute of Physics and an AFRL Fellow.

Thomas R. Harris received his PhD in applied physics from the Air Force Institute of Technology in 2014. He has worked in the Optoelectronic Technology Branch of the Air Force Research Laboratory, Sensors Directorate at Wright–Patterson Air Force Base since 2015, first as an NRC postdoctoral research associate and more recently as a contractor with Azimuth Corp. His interests include infrared spectroscopy and transition-metal and rare-earth-doped laser host materials.

Kenneth L. Schepler received his BS degree in physics from Michigan State University and MS and PhD degrees from the University of Michigan. He was a research physicist at the Air Force Research Laboratory (AFRL) at Wright–Patterson Air Force Base for more than 32 years. He retired in 2014 and is now a research professor at CREOL. His research interests include solid state lasers, laser spectroscopy, and nonlinear frequency conversion. He is a fellow of Optica and AFRL.